Title

Increasing Photoluminescence Quantum Yield by Nanophotonic Design of Quantum-Confined Halide Perovskite Nanowire Arrays

Journal

Nano Letters, 19(5)

ISSN

1530-6984

Authors

Zhang, Daquan
Gu, Leilei
Zhang, Qianpeng
et al.

Publication Date

2019-05-08

DOI

10.1021/acs.nanolett.8b04887

Peer reviewed

Increasing photoluminescence quantum yield by nanophotonic design of quantum-confined halide perovskite nanowire arrays

Daquan Zhang[1], Leilei Gu[1], Yuanjin Lin[1, 2], Qianpeng Zhang[1], Der-Hsien Lien[2], Matthew Kam[1], Swapnadeep Poddar[1], Erik C. Garnett[3], Ali Javey[2], Zhiyong Fan[1*]

[1]*Department of Electronic and Computer Engineering, The Hong Kong University of Science and Technology, Clear Water Bay, Kowloon, Hong Kong SAR, China*

[2]*Electrical Engineering and Computer Sciences, University of California, Berkeley, California 94720, USA*

[3]*Center for Nanophotonics, AMOLF, Science Park 104, 1098 XG Amsterdam, The Netherlands*

[*]*Corresponding author*: eezfan@ust.hk

High photoluminescence quantum yield (PLQY) is required to reach optimal performance in solar cells, lasers and light-emitting diodes. Typically, PLQY is increased by improving the material quality to reduce the non-radiative recombination rate. It is in principle equally effective to improve the optical design by nanostructuring a material to increase light out-coupling efficiency and introduce quantum confinement, both of which can increase the radiative recombination rate. However, increased surface recombination typically minimizes nanostructure gains in PLQY. Here we demonstrate that porous alumina membranes can be used to control the diameter of $CH_3NH_3PbI_3$ nanowire arrays from the bulk (250 nm) to the quantum-confined regime (5.7 nm), while simultaneously providing a low surface recombination velocity of 18 cm/s. This enables the 54-fold increase in radiative recombination rate and 2.2-fold increase in light out-coupling efficiency to increase the PLQY by a factor of 130, from 0.33% up to 42.6%, exclusively using nanophotonic design.

Photoluminescence quantum yield (PLQY) is defined as the fraction of absorbed photons that are converted to external emission. It is determined by the relative rates of radiative and non-radiative recombination and thus plays a key role in the performance of a wide variety of optoelectronic devices such as solar cells[1,2], light-emitting diodes[3-5] and lasers[6]. The common approach to

increase PLQY is to improve material quality, which reduces the non-radiative recombination rate, for example by minimizing bulk[7], surface[8] and interfacial[9] defects. It is in principle also possible to increase PLQY solely via nanophotonic engineering, by increasing the absorption cross-section[10], light outcoupling[11] or quantum confinement[12]. All of these strategies increase the radiative recombination rate, but very often the increase in surface recombination when nanostructuring a material plays a bigger role, leading overall decreases in PLQY. In the most successful example so far, nanostructuring InP increased PLQY by a factor of 14 using a combination of increased absorption cross-section and light outcoupling[13]. Such a large improvement was enabled by the very low native surface recombination velocity of InP as well as its high refractive index, which leads to low light out-coupling efficiency (2%) in planar wafers due to total internal reflection. Increasing light out-coupling has also been applied to halide perovskite materials, but the lower refractive index makes it more difficult to see an improvement – indeed only a factor of 3 has been observed so far.[14] However, halide perovskites also have very low native surface recombination velocity[15], making them an interesting candidate for studying radiative recombination rate enhancements via quantum confinement. Several studies have observed quantum confinement in colloidal halide perovskite nanowires (NWs)[16-18]. In one case, smaller diameters led to lower PLQY, showing that surface recombination dominated over the quantum confinement effect[16]. In the other example, a substantial increase in PLQY by a factor of 6 was observed[17], but different synthetic conditions used to reach different NW diameters made it difficult to determine the relative effect of quantum confinement versus differences in material quality. Furthermore, colloidal systems are not suitable for most optoelectronic applications, where quantum wires (QWs) need to be in the solid-state in a geometry that allows for contacting. It is thus an outstanding challenge to synthesize QWs with tunable diameters suitable for fundamental studies and optoelectronic device applications, while equally challenging is reaching sufficiently excellent surface passivation so that the change in radiative recombination rate rather than surface recombination dominates the PLQY.

Here we solve both the synthetic and surface passivation challenges enabling a 130-fold increase in PLQY only via reducing the NW diameter, by far the largest report originating exclusively from nanophotonic effects. We utilize porous alumina membranes (PAMs) as templates to fabricate ultra-high density (~$1x10^{12}$ cm^{-2}) vertical $CH_3NH_3PbI_3$ NW arrays with controllable and uniform diameters from 250 ± 10 nm down to 5.7 ± 1.4 nm, all grown under the same vapor-solid-solid

reaction (VSSR) conditions.[19-21] The processes for PAM formation, VSSR growth, photodetector fabrication, and extraction of QWs for transmission electron microscopy (TEM) characterization are shown schematically in **Fig. 1 (full details in Methods)**. Briefly, the nano-engineered PAMs are formed by electrochemical anodic anodization of aluminum (Al) foil, with the pore diameter in nanometers approximately equal to the anodization voltage in Volts (**Fig. S1, S2**). After a barrier layer breakthrough etch, metallic lead (Pb) is electrochemically deposited at the bottom of the PAM channels and subsequently converted to $CH_3NH_3PbI_3$ NW arrays using the VSSR process.[19] A variety of perovskite NWs can be obtained with a similar process simply by electrodepositing different metals at the bottom of the PAM[20] or by using different powder precursors during the growth.[21] A low energy surface ion milling process is carried out to remove the unwanted layer of bulk polycrystalline $MAPbI_3$ on the top of the PAM, leading to NWs with identical length in all PAM nanochannels. Afterwards, another short growth step using the same conditions is used to repair the ion beam damaged surface. All optical measurements are performanced on the arrays at this stage (**Fig. 1e**). For the photodetector measurements, patterned indium-tin-oxide (ITO) contacts are sputtered on top of the NW arrays (**Fig. 1f**).

The PAM serves as an excellent packaging material for halide perovskite NWs, leading to drastically improved stability against water, oxygen and spontaneous phase transformation.[17] This stability enhancement is critical for device applications, but also makes it difficult to extract individual NW for TEM characterization. Since etching away the PAM with acids/bases would destroy the perovskite NW array, we instead mechanically grind the embedded array into a fine powder (**Fig. 1g**) and subsequently sonicate it in chlorobenzene. The sonication extracts the NWs from the broken edges of the PAM and uniformly disperses them in the solvent (**Fig. 1h**), enabling TEM characterization as well as future single QWs device fabrication and characterization.

High-resolution TEM (HRTEM) and X-ray diffraction (XRD) confirm that the $CH_3NH_3PbI_3$ NWs are monocrystalline (**Fig. 2**). Interestingly, the XRD patterns are dominated by (100) planes, indicating the NWs adopt a cubic crystal structure [19,22], corresponding to the high temperature phase (>327 K) of bulk $CH_3NH_3PbI_3$ [23]. Meanwhile, the obvious decreasing in signal intensity and broadening of the diffraction peaks is consistent with the QW diameter reduction, as also seen with colloidal perovskite quantum dots (QDs) [24] and QWs [16]. From the HRTEM, it is clear that both the electrodeposited Pb and the converted $CH_3NH_3PbI_3$ NWs have diameters determined

entirely by the PAM (**Fig. 2 and S3**). The inter-planar distance of ~0.63 nm corresponds to (100) planes of cubic $MAPbI_3$, just as been observed with nanocrystals.[25]

Absorption and photoluminescence spectra show that the 250 nm diameter NW arrays exhibit optical properties comparable to those of bulk $MAPbI_3$ (**Fig. 3a),**[19] while as the diameter decreases towards the Bohr radius, the PL peak and absorption edge show a significant blue-shift, indicating bandgap widening due to quantum confinement. Especially, compared with the PL peak and absorption edge of 772 nm for 250±10 nm diameter NW arrays, the 5.7±1.4 nm diameter QW arrays show a maximum 59 nm (133 meV) blue shift. Note that recently, a maximum 122 nm (301.5 meV) blue shift was observed from $MAPbI_3$ QDs with almost the same diameter (6.6± 0.7nm) [26]**.** This discrepancy can be explained by the fact that QWs have only 2-D confinement of excitons while QDs have stronger 3-D confinement.[27] **Fig. 3b** quantitatively illustrates the dependence of optical bandgap on the average NW diameter, calculated using the PL peak position. The bandgap change (ΔE_g) shows an inverse square relationship ($\Delta E_g \propto 1/d^2$) to the diameter (d), consistent with the simple particle-in-a-box model for QWs:[27-29]

$$\Delta \mathrm{E}_g = \frac{1.17h^2}{8d^2} \cdot \left(\frac{1}{m_e^*} + \frac{1}{m_h^*}\right) = \frac{1.17h^2}{8m^* d^2} = \frac{k}{d^2}, \quad (1)$$

where, h, m_e^*, m_h^*, and m^* reprensent Planck's constant and the electron, hole and reduced effective mass, respectively. Using the slope value (k) of 2.70 eV·nm^2 extracted from the linear fitting (**Fig. 3b** inset), the reduced effective mass m^* is estimated to be $0.16m_0$, where m_0 is the free electron mass. This result is consistent with the reported value of $0.15m_0$.[30]

Fig. 3d shows that as the NW diameter decreases from 250 nm to 5.7 nm, the PLQY increases from 0.33% to 42.6%. In all cases the PLQY is nearly independent of excitation intensity, with a maximum increase by a factor 4 when changing the intensity by 4 orders of magnitude. This suggests all NW samples are in the low-injection regime, where the background carrier density is much higher than the photogenerated carrier density.[3] The situation is very different for the thin film, which not only shows a lower PLQY (maximum of 0.1%), but also a strong power dependence, approaching the linear scaling expected for films dominated by non-radiative recombination in the high injection regime.[31] The large difference likely arises from the different synthetic methods between the thin-film and NW arrays. The increase in PLQY with stronger quantum confinement suggests the origin of the improvement is an increased radiative

recombination rate (nanophotonic effect), rather than a decreased non-radiative recombination rate (improved material). Time-resolved photoluminescence (TRPL) measurements confirm this hypothesis, showing that smaller diameter NWs have faster PL decays (see Methods fitting details), corresponding to shorter carrier lifetimes (**Fig. 3c**, **Table 1**). Combining the PLQY and lifetime data measured at the same incident photon flux allows us to extract both the radiative and non-radiative recombination rates as a function of NW diameter (see Methods for details).

Fig. 3e plots the radiative recombination rate versus the inverse NW diameter squared. Above a diameter of 12 nm, the radiative recombination rate is nearly constant, while it increases linearly below this threshold diameter, ultimately reaching a value at 5.7 nm that is 54 times higher than that at 250 nm. As the NW diameter shrinks, we also expect the non-radiative recombination rate to increase due to enhanced surface recombination.[32] Plotting the non-radiative recombination rate versus the NW surface-to-volume ratio (2/r) allows us to extract a surface recombination velocity (SRV) of 18 cm/s from the slope of the linear fit (**Fig. 3f**).[33] Besides increasing the radiative recombination rate via quantum confinement and increasing the surface recombination rate, decreasing the NW diameter also is expected to increase the light outcoupling[34]. In order to quantify this, we simulated the light out-coupling efficiency of dipoles with different orientations and positions in the NW arrays as a function of diameter (**Fig. S4**). **Table 1** shows the average values, demonstrating that reducing the NW diameter from 250 nm to 5.7 nm increases the light out-coupling by a factor of 2.2, further contributing to the enhanced PLQY. Finally, the PAM also increases the stability of the embedded NWs. **Fig. 3g** plots the PLQY of QWs, large diameter NWs and the thin film over a period of 7 days. Note the PLQYs are normalized for ease of comparison. It can be seen that, after being stored in ambient condition without any additional packaging (temperature: 23^{o}C, relative humidity: 18%-40%) for 7 days, the PLQY of the thin film, NWs and QWs decreased to ~24%, ~71%, and 80%, respectively, of the original value (day 0). This suggests that the QWs have the best stability as compared with the thin film and NWs. And this significantly improved material stability can be attributed to the PAM template's effective protection against water and oxygen molecules in ambient conditions.[20]

High quality perovskite QWs with superior properties and stability are promising for optoelectronic device applications such as light-emitting diodes and photodetectors with tunable spectral response. However, due to the material stability issue and incompatibility with

nanofabrication processes, device fabrication using individual QWs remains a challenge. However, our ultra-high density (~10^{12} cm^{-2}) vertical QW arrays can be simply integrated with contacts to create photodetectors. In such a device, the Al substrate and the layer of 100 nm transparent ITO serve as the bottom and top electrodes respectively. The schematic band energy diagrams for zero, forward, and reverse biases are shown in **Fig. S5**. Under zero bias, the photo-generated electro-hole pairs cannot be easily collected by the electrodes because of the existence of the Al_2O_3 barrier layer between the Al electrode and the QWs. However, when applying high enough bias, carriers can tunnel through the barrier layer and lead to a large tunneling current. This asymmetric contact structure leads to a Schottky junction, which can be observed in the I-V curves under dark and white halogen light (11.2 mW/cm^2) illumination (**Fig. 4a and S6). Fig. 4b** characterizes the time-domain light response under -5 V bias and pulsed light for QW arrays. Although the performance is not ideal, it should be possible to enhance the current collection by using shorter QWs and by removing Al_2O_3 barrier layer completely.[19] The typical response speed of the device is extracted from the I-t curve shown in **Fig. 4c**. The photocurrent rise time (t_{rise}) of 80 ms and fall time (t_{fall}) of 140 ms are reasonably short, and can also be further improved by reducing the QW length to reduce the resistance and charge-carrier collection time and by shrinking the top electrode area to reduce the parasitic capacitance between the two electrodes. Finally, the wavelength-dependent responsivity is characterized and shown in **Fig. 4d**. In this case, the 5.7 ± 1.4 nm QW array device was used for measurement, and the same -5 V bias was applied during the measurement. It can be seen that the photo responsivity suddenly drops from 1.23 mA/W to ~0 when the incident optical wavelength increases from 720 nm to 730 nm, which is in excellent agreement with the absorption edge and PL emission peak shown in **Fig. 3a**.

We see that PAMs provide a flexible platform for studying fundamental nanophotonic effects such as quantum confinement and light out-coupling, while also bringing the practical benefits of outstanding surface passivation, improved stability and simple contacting for optoelectronic devices. From a fundamental perspective, this study demonstrates that PLQY can be enhanced by a factor of 130 purely using nanophotonic design, rather than the traditional approach of improving the quality of the material, surfaces or interfaces. Combining the PLQY and PL decay measurements at the same excitation intensity allows us to quantify the contributions of quantum confinement and light out-coupling as well as measure the SRV. The 54-fold increase in radiative recombination rate combined with the 2.2-fold increase in light out-coupling, agrees quantitatively

with the 130-fold increase in PLQY. The outstanding SRV of 18 cm/s is comparable to state-of-the-art Si passivation, and is a necessary enabling condition to observe the enormous PLQY improvements. Although the first photodetector shows modest performance, the ease of fabrication combined with the outstanding optoelectronic properties and improved stability make this geometry very promising for future testing in solar cells and LEDS. The spontaneously formed honeycomb lattice provides opportunities to further exploit nanophotonic effects using photonic crystal modes, perhaps even for electrically-injected lasers. The simple extension of this technique to a wide variety of perovskite materials and the ultra-high density of vertical QWs may also provide interesting opportunities in quantum transport, electronics and memory devices in the future.

References

1. Akkerman, Q. A., Gandini, M., Stasio, F. D., Rastogi, P., Palazon, F., Bertoni, G., Ball, J. M., Prato, M., Petrozza, A. & Manna, L. Strongly emissive perovskite nanocrystal inks for high-voltage solar cells. *Nat. Energy* **2**, 16194 (2016).

2. Carey, G. H., Abdelhady, A. L., Ning, Z. J., Thon, S. M., Bakr, O. M. & Sargent, E. H. Colloidal quantum dot solar cells. *Chem. Rev.* **115**, 12732-12763 (2015).

3. Yuan, M. J., Quan, L. N., Comin, R., Walters, G., Sabatini, R., Voznyy, O., Hoogland, S., Zhao, Y. B., Beauregard, E. M., Kanjanaboos, P., Lu, Z. H., Kim, D. H. & Sargent, E. H. Perovskite energy funnels for efficient light-emitting diodes. *Nat. Nanotech.* **11**, 872-877 (2016).

4. Chiba, T., Hayashi, Y., Ebe, H., Hoshi, K., Sato, J., Sato, S., Pu, Y. J., Ohisa, S. & Junji K. Anion-exchange red perovskite quantum dots with ammonium iodine salts for highly efficient light-emitting devices. *Nat. Photonics* (2018).

5. Lin, K. B., Quan, L. N., Arquer, F. P. G., Gong, X. W., Lu, J. X., Xie, L. Q., Zhao, W. J., Zhang, D., Yan, C. Z., Li, W. Q., Liu, X. Y., Lu, Y., Kirman, J., Sargent, E. H., Xiong, Q. H. & Wei, Z. H. Perovskite light-emitting diodes with external quantum efficiency exceeding 20 per cent. *Nature* **562**, 245-247 (2018).

6. Veldhuis, S. A., Boix, P. P., Yantara, N., Li, M. J., Sum, T. C., Mathews, N. & Mhaisalkar, S. G. Perovskite materials for light-emitting diodes and lasers. *Adv. Mater.* **28**, 6804-6834 (2016).

7. Shi, D., Adinolfi, V., Comin, R., Yuan, M. J., Alarousu, E., Buin, A., Chen, Y., Hoogland, S., Rothenberger, A., Katsiev, K., Losovyj, Y., Zhang, X., Dowben, P. A., Mohammed, O. F., Sargent, E. H. & Bakr, O. M. Low trap-state density and long carrier diffusion in organolead trihalide perovskite single crystals. *Science* **347**, 519-522 (2015).

8. Marino, E., Kodger, T. E., Crisp, R. W., Timmerman, D., MacArthur, K. E., Heggen, M. & Schall, P. Repairing nanoparticle surface defects. *Angew. Chem.* **129**, 13983-13987 (2017).

9. Chen, M. X., Liu, Y., Li, C. C., Li, A., Chang, X. X., Liu, W., Sun, Y., Wang, T. & Gong, J. L. Spatial control of cocatalysts and elimination of interfacial defects towards efficient and robust CIGS photocathodes for solar water splitting. *Energy Environ. Sci.* **11**, 2025-2034 (2018).

10. Xu, W. W., Hou, X. Q., Meng, Y. J., Meng, R. Y., Wang, Z. Y., Qin, H. Y., Peng, X. G. & Chen, X. W. Deciphering charging status, absolute quantum efficiency, and absorption cross section of multicarrier states in single colloidal quantum dots. *Nano Lett.* **17**, 7487-7493 (2017).

11. Lien, D. H., Kang, J. S., Amani, M., Chen, K., Tosun, M., Wang, H. P., Roy, T., Eggleston, M. S., Wu, M. C., Dubey, M., Lee, S. C., He, J. H. & Javey, A. Engineering light outcoupling in 2D materials. *Nano Lett.* **15**, 1356-1361 (2015).

12. Buhro, W. & Colvin, V. Semiconductor nanocrystals Shape matters. *Nat. Mater.* **2**, 138-139 (2003).

13.

14. Richter, J. M., Abdi-Jalebi, M., Sadhanala, A. S., Tabachnyk, M., Rivett, J. P. H., Pazos-Outón, L. M., Gödel, K. C., Price, M., Deschler, F. & Friend, R. H. Enhancing photoluminescence yields in lead halide perovskites by photon recycling and light out-coupling. *Nat. Commun.* **7**, 13941 (2016).

15. Yang, Y. Yan, Y., Yang, M. J., Choi, S., Zhu, K., Luther, J. M. & Beard, M. C. surface recombination velocity. *Nat. Commun.* **6**, 7961 (2015).

16. Teunis, M.; Jana, A.; Dutta, P.; Johnson, M.; Mandal, M.; Muhoberac, B. & Sardar, R. Mesoscale Growth and Assembly of Bright Luminescent Organolead Halide Perovskite Quantum Wires. *Chem. Mater.* **28**, 5043-5054 (2016).

17. Imran, M.; Stasio, F.; Dang, Z.; Canale, C.; Khan, A.; Shamsi, J.; Brescia, R.; Prato, M. & Manna, L. Colloidal Synthesis of Strongly Fluorescent CsPbBr3 Nanowires with Width Tunable down to the Quantum Confinement Regime. *Chem. Mater.* **28**, 6450-6454 (2016).

18. Zhang, D. D., Yu, Y., Bekenstein, Y., Wong, A. B., Alivisatos, A. P., & Yang, P. D. Ultrathin Colloidal Cesium Lead Halide Perovskite Nanowires. *J. Am. Chem. Soc.* **138**, 13155–13158 (2016).

19. Gu, L. L.; Tavakoli, M.; Zhang, D. Q.; Zhang, Q. P.; Waleed, A.; Xiao, Y.; Tsui, K.; Lin, Y. J.; Liao, L.; Wang J. N. & Fan, Z. Y 3D Arrays of 1024 - Pixel Image Sensors based on Lead Halide Perovskite Nanowires. *Adv. Mater.* **28**, 9713-9721 (2016).

20. Waleed, A.; Tavakoli, M.; Gu, L. L.; Wang Z. Y.; Zhang, D. Q.; Manikandan, A.; Zhang, Q. P.; Zhang, R.; Chueh, Y. & Fan, Z. Y. Lead-Free Perovskite Nanowire Array Photodetectors with Drastically Improved Stability in Nanoengineering Templates. *Nano lett.* **17**, 523-530 (2017).

21. Waleed, A.; Tavakoli, M.; Gu, L. L.; Hussain, S.; Zhang, D. Q.; Poddar, S.; Wang, Z. Y.; Zhang, R. J. & Fan, Z. All Inorganic Cesium Lead Iodide Perovskite Nanowires with Stabilized Cubic Phase at Room Temperature and Nanowire Array-Based Photodetectors. *Nano Lett.* **17**, 4951-4957 (2017).

22. Burschka, J.; Pellet, N.; Moon, S.-J.; Humphry-Baker, R.; Gao, P.; Nazeeruddin, M.; Grätzel, M. Sequential deposition as a route to high-performance perovskite-sensitized solar cells. *Nature* **499**, 316-319 (2013).

23. Singh, R. K.; Kumar, A.; Jain, N.; Singh, J.; Singh, R. K. & Kumar, R. Solution Processed Hybrid Organic-Inorganic CH3NH3PbI3 Perovskite Material and Optical Properties. *Mater. Today: Proc.* **4**, 12661-12665 (2017).

24. Zhang, F.; Zhong, H.; Chen, C.; Wu, X.; Huang, H.; Han, J.; Zou, B. & Dong, Y. Brightly Luminescent and Color-Tunable Colloidal CH3NH3PbX3 (X = Br, I, Cl) Quantum Dots: Potential Alternatives for Display Technology. *ACS Nano* **9**, 4533-4542 (2015).

25. Zushi, M.; Suzuki, A.; Akiyama, T.; Oku, T. Fabrication and Characterization of TiO2/CH3NH3PbI3-based Photovoltaic Devices. *Chem. Lett.* **43**, 916-918 (2014).

26. Zhang, F.; Huang, S.; Wang, P.; Chen, X.; Zhao, S.; Dong, Y.; Zhong, H. Colloidal Synthesis of Air-Stable CH3NH3PbI3 Quantum Dots by Gaining Chemical Insight into the Solvent Effects. *Chem. Mater.* **29**, 3793-3799 (2017).

27. Yu, H.; Li, J.; Loomis, R.; Wang, L. & Buhro, W. Two- versus three-dimensional quantum confinement in indium phosphide wires and dots. *Nat. Mater.* **2**, 517-520 (2003).

28. Gudiksen, M.; Wang, J. & Lieber, C. Size-Dependent Photoluminescence from Single Indium Phosphide Nanowires. *J. Phys. Chem. B* **106**, 4036-4039 (2002).

29. Nanda, K.; Kruis, F. & Fissan, H. Energy Levels in Embedded Semiconductor Nanoparticles and Nanowires. *Nano Lett.* **1**, 605-611 (2001).

30. Tanaka, K.; Takahashi, T.; Ban, T.; Kondo, T.; Uchida, K. & Miura, N. Comparative study on the excitons in lead-halide-based perovskite-type crystals CH3NH3PbBr3 CH3NH3PbI3. *Solid State Commun.* **127**, 619-623 (2003).

31. Ymamada, Y., Nakamura, T., Endo, M., Wakamiya, A. & Kanemitsu, Y. Photocarrier Recombination Dynamics in Perovskite CH3NH3PbI3 for Solar Cell Applications. *J. Am. Chem. Soc.* **136**, 11610−11613 (2014).

32. Dan, Y. P., Seo, K., Takei, K., Meza, J. H., Javey, A. & Crozier K. B. Dramatic Reduction of Surface Recombination by in Situ Surface Passivation of Silicon Nanowires. *Nano Lett.* **11**, 2527–2532 (2011).

33. Khoram, P., Oener, S. Z., Zhang, Q. P., Fan, Z. Y. & Garnett, E. C. Surface recombination velocity of methylammonium lead bromide nanowires in anodic aluminium oxide templates. *Mol. Syst. Des. Eng.* **3**, 723-728 (2018).

34. Babinec, T. M., Hausmann, B. J. M., Khan, M., Zhang, Y. N., Maze, J. R., Hemmer, P. R. & Lončar, M. A diamond nanowire single-photon source. *Nat. Nanotech.* **5**, 195-199 (2010).

Acknowledgements

This work was supported by the National Natural Science Foundation of China (project 51672231) and the General Research Fund (Project No. 612113 and 16237816) from the Hong Kong Research Grant Council. The authors acknowledge the support received from the Center for 1D/2D Quantum

Materials and State Key Laboratory on Advanced Displays and Optoelectronics at HKUST. D. Zhang acknowledges the technical assistance from Miss Jenny Kontoleta from Center for Nanophotonics, AMOLF Amsterdam, The Netherlands.

Author contributions

Z. F. conceived the ideas and supervised the work; D. Z. prepared the NWs/QWs samples and carried out optical spectroscopy, XRD, SEM, and TEM characterizations; Y. L., D. L., and A. J. carried out the PLQY measurement; Q. Z. carried out optical simulations of the samples; M. K. prepared the thin film samples; D. Z. fabricated and characterized the photodetector devices with the assistance of L. G., Q. Z., and S. P;.D. Z., E. G. A. J. and Z. F. carried out the data analysis and wrote the manuscript. All authors discussed the results and commented on the manuscript.

Competing interests

The authors declare no competing interests.

Methods

PAM fabrication. The PAMs were fabricated by using a well-known anodic anodization with low voltages. Briefly, after being cleaned with acetone and isopropyl alcohol, a high purity Al foil with around 1.5 x 2.5 cm size was electrochemically polished in an acidic solution made from 25 vol% $HClO_4$ and 75 vol% CH_3CH_2OH for 2.5 min under 12.5 V at room temperature. Afterward, the first anodic anodization was carried out by immersing the Al chip into acid solution (5 vol% H_2SO_4) under different DC voltages (5 V, 10 V, 15 V, and 20 V) at 10^{o}C for different time (24 hours, 12 hours, 5 hours, and 3 hours, respectively). Followed by the second anodization with the same condition, an acid etching (6 wt% H_3PO_4 and 1.8 wt% CrO_3) of the first anodization layer was carried out at 98 ^{o}C for 15 min. To get 100nm thick PAM in the second anodization, it empirically took around 20min, 10min, 2min, and 1min for 5 V, 10 V, 15 V, and 20 V anodization, respectively. At the end of the second anodization (except for the 5 V one), the DC voltage source mode was directly switched to DC current source mode with current value being half of that in voltage mode, which would trigger a voltage-ramping-down process and hence thin down the barrier layer at the bottom of PAM channels. When the voltage reached 5 V, the process was

terminated and the PAM chips were rinsed with deionized (DI) water and dried with compressed air for the later use.

Pb electrodeposition. The Pb precursor was electrochemically deposited at the bottom of PAM nano-channels in aqueous electrolyte made from 1.7 g of $PbCl_2$, 25 g of trisodium citrate and 100 mL DI water. A potentiostat (SG 300, Gamry instruments) was used to supply a sinusoidal voltage signal with 60 Hz frequency and 5 V amplitude for 10 s. Nano-crystaline Pb NWs would be consequently obtained at the bottom of PAM channels.

$MAPbI_3$ QWs growth and photodetector device fabrication. The $MAPbI_3$ QWs were synthesized through the reaction between Pb and MAI vapor as reported earlier. [19] Briefly, the PAM chip with Pb NWs deposited was placed into the face-to-face glass bottles with MAI powder inside, which helps to trap the MAI vapor and hence promotes the reaction. A tube furnace (1-inch diameter size) with Ar carrier gas was then used to heat them up to 180 ^oC for 5 min to completely consume Pb precursor. To guarantee all QWs having identical length, excess Pb precursor was deposited beforehand to make sure there is a layer of $MAPbI_3$ thin film on the top surface of PAM template, and successively a surface ion milling process and regrowth were carried out to remove the polycrystalline thin film. Specifically, in the 1 hour ion milling process, argon ions were accelerated by 100 V voltage in a vacuum of $1.4x10^{-4}$ torr. The angle between the ion acceleration path and the normal of the chip is 80^o with continuous rotation of the chip during the etching. Afterward, another VSSR process with the same growth condition was carried out but only for 30 s to repair the ion beam damaged surface. To fabricate a photodetector device, a transparent 100nm layer of ITO was sputtered on top of substrate using a circle shadow mask of 0.0314 cm^2 area.

Single Pb NW and $MAPbI_3$ QW extraction. To extract a single $MAPbI_3$ QW out from the PAM template for TEM, a mechanical grinding and sonication process was utilized. Followed by the $MAPbI_3$ QWs growth, a free-standing PAM membrane with deposited Pb NWs was obtained by $HgCl_2$ etching.[19] Afterward, the membrane was mechanically grinded into fine powder, dissolved in chlorobenzene, and sonicated for 20 min, which finally would extract QWs out from the edge of broken PAM pieces and uniformly dispersed them into the solvent. The Pb NWs extraction was carried out by using the same process except for the $MAPbI_3$ QWs growth step.

Characterization. SEM images of PAM were characterized using a field-emission scanning electron microscopy (JEOL JSM-7800F). XRD patterns of $MAPbI_3$ QW arrays in PAM were

obtained using Bruker D8 X-ray diffracttometer. TEM images were obtained by TEM JEOL (2010) with 200 kV acceleration voltage. UV-vis absorption and PL including spectrum, lifetime, and QY were measured using Varian Cary 500 spectrometer (Varian, USA) and Edinburgh FS5 flourescence spectrometer, respectively. A double-exponential function was used to fit all PL decay profiles:

$$I(t) = A + B_1 e^{(-t/\tau_1)} + B_2 e^{(-t/\tau_2)}, \quad (2)$$

with fitting results shown in **Table S1**. The average lifetime (used to calculate radiative and non-radiative recombination rates) is given by: $\tau_{ave} = \frac{\tau_1 * B_1 + \tau_2 * B_2}{B_1 + B_2}$.

The PLQY (η) can be written as;

$$\eta = \frac{R_{rad}}{R_{rad} + R_{nrad}} = \frac{R_{rad}}{R_{total}} \quad (3)$$

where R_{rad}, R_{nrad} and R_{total} are radiative, non-radiative and total recombination rates, respectively. Hence, considering the relation between R_{total} and τ_{ave}:

$$R_{total} = 1/\tau_{ave} \quad (4)$$

the diameter (d) or radius (r)-dependent radiative and non-radiative recombination rates can be easily calculated as:

$$R_{rad}(d) = \eta(d)/\tau_{ave}(d) \quad (5)$$

$$R_{nrad}(r) = (1 - \eta(r))/\tau_{ave}(r) \quad (6)$$

It is important to use the same injection levels for the lifetime and PLQY measurements for this calculation, so the laser excitation power density is 0.1 mW/cm^2 for both.

The photodector device was characterized using a HP 4156A Analyzer along with probe station (Singatone, US) and broadband Halogen lamp as a light source.

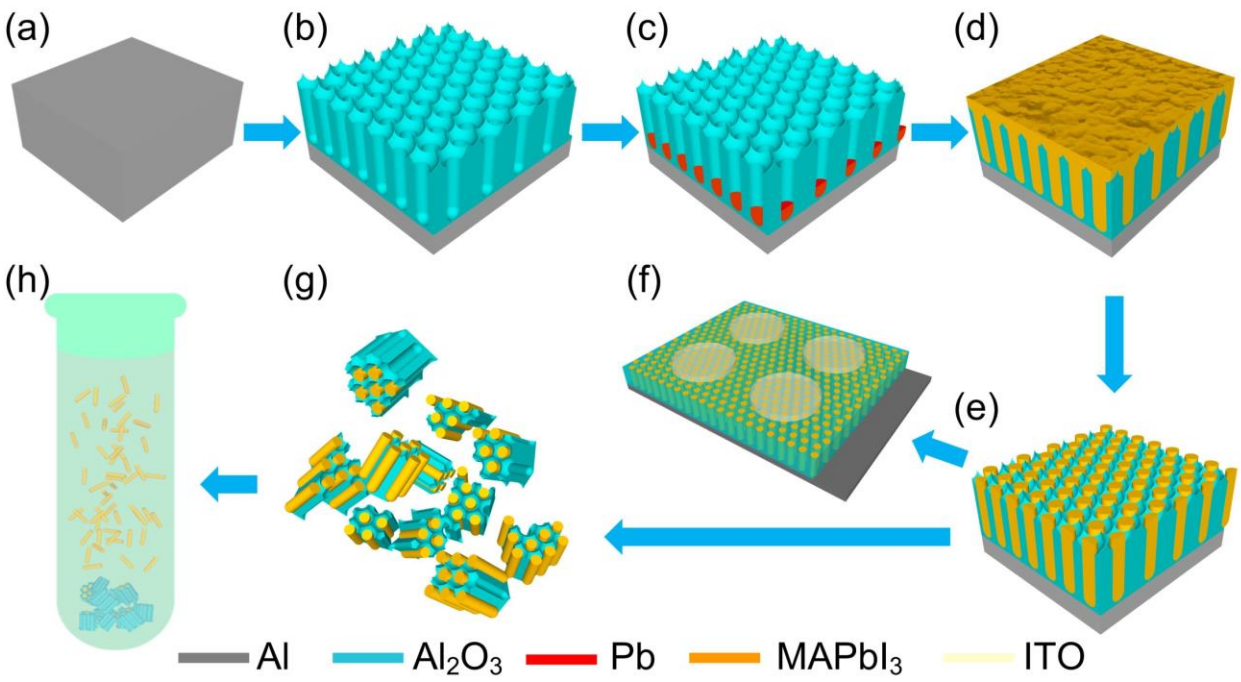

Figure 1. Schematic of PAM template assisted growth of $MAPbI_3$ QW arrays for single QW extraction and photodetector fabrication.

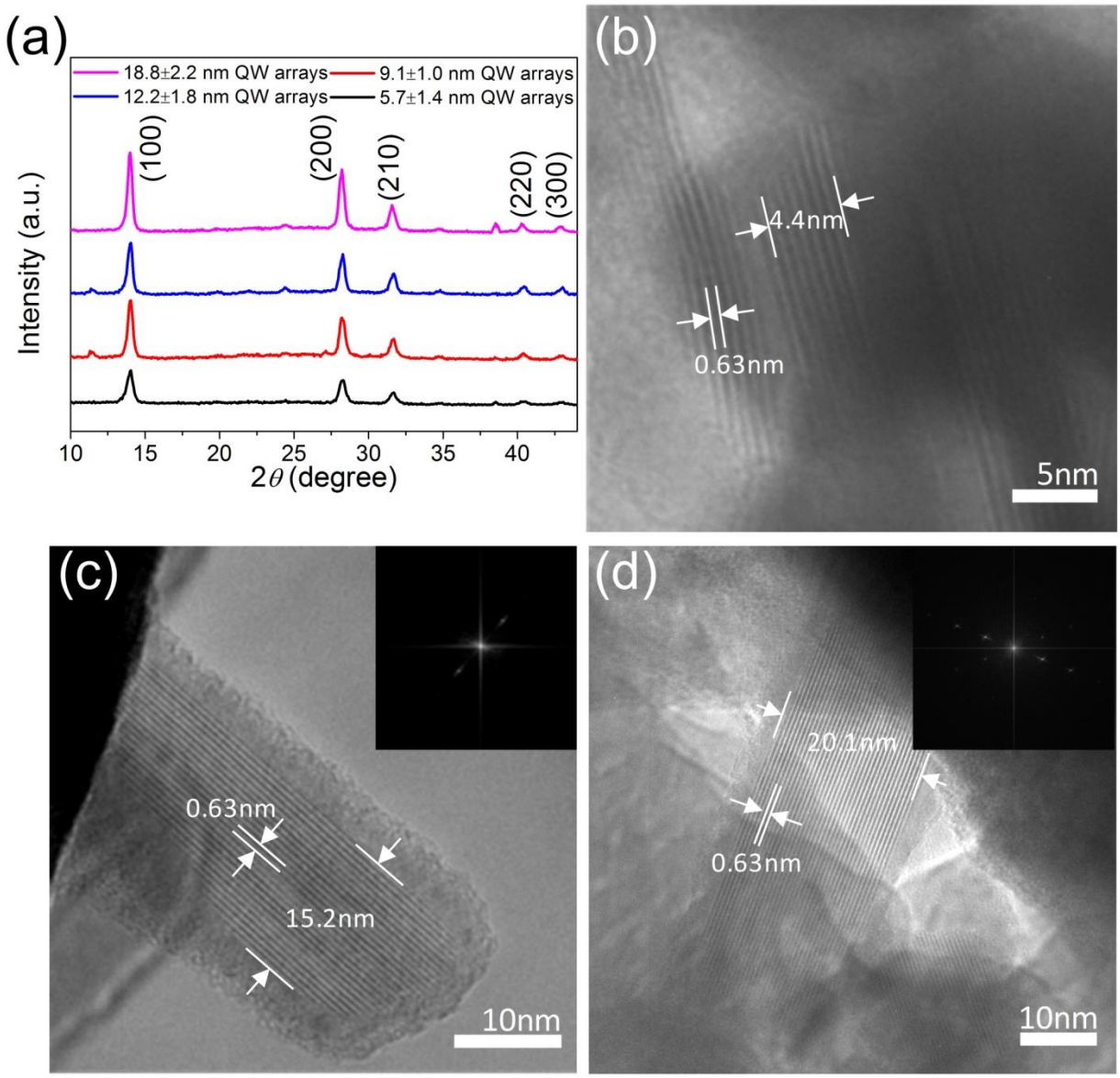
(a)
18.8±2.2 nm QW arrays
9.1±1.0 nm QW arrays
12.2±1.8 nm QW arrays
5.7±1.4 nm QW arrays
(100)
(200)
(210)
(220)
(300)
Intensity (a.u.)
10
15
20
25
30
35
40
2θ (degree)
(b)
4.4nm
0.63nm
5nm
(c)
0.63nm
15.2nm
10nm
(d)
20.1nm
0.63nm
10nm

Figure 2. (a) XRD patterns of $MAPbI_3$ QW arrays in 5 V(black curve), 10 V(red curve), 15 V(blue curve), and 20 V(pink curve) PAM. TEM images of $MAPbI_3$ QWs extracted from (b)5 V, (c)15 V and (d)20 V PAM. The insets show the corresponding FFT analysis.

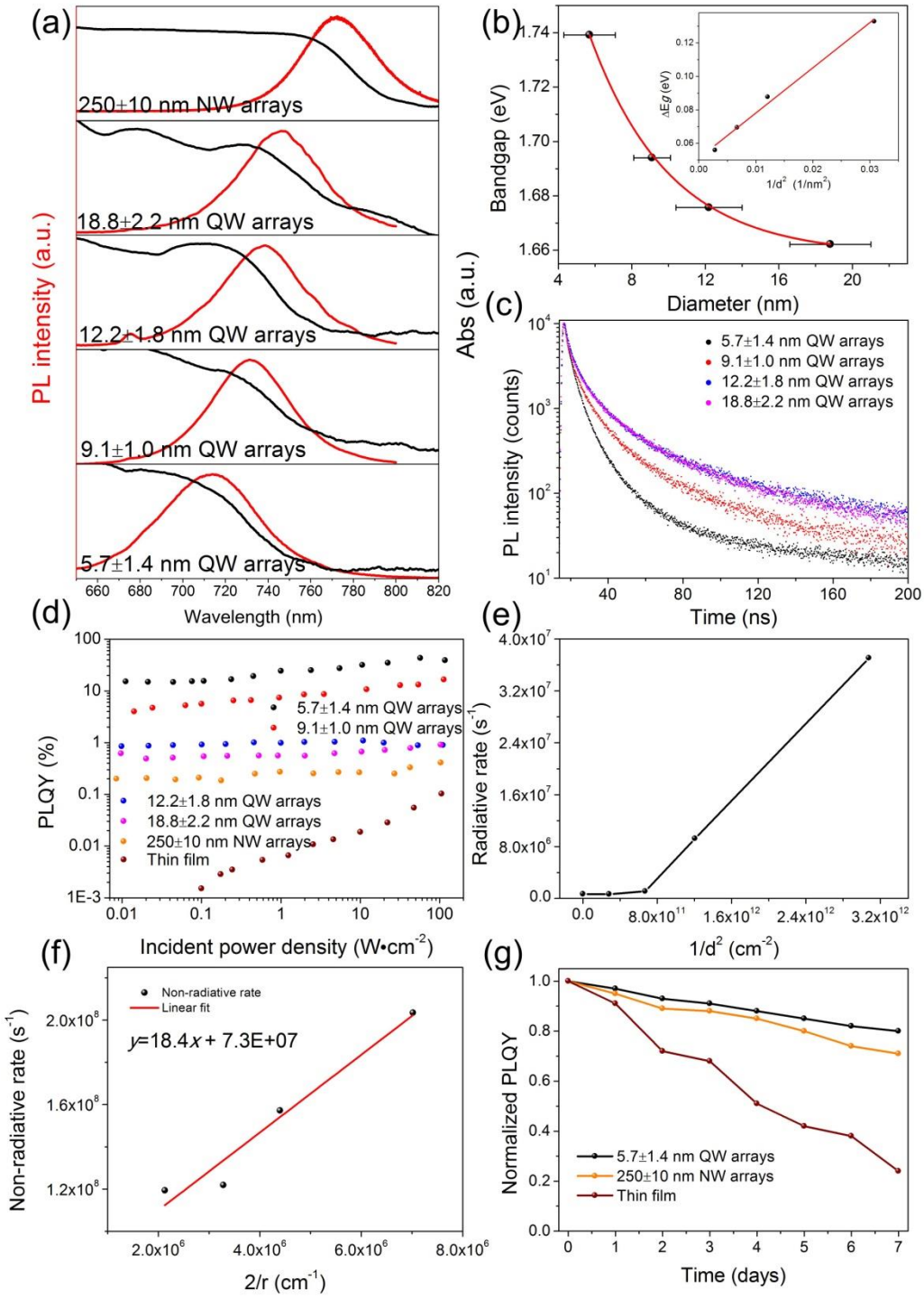

Figure 3. (a) Normalized PL spectra (λ_{ex}=400nm) of $MAPbI_3$ QW arrays in different AAO templates and MAPbI3 NW arrays, showing maximum 59nm PL peak blue shift. (b) Dependence of calculated bandgap on the QW diameter. The insert: the linear fitting of bandgap change versus $1/d^2$. (c) TRPL (λ_{ex}=365nm) measured at the PL peak for $MAPbI_3$ QWs with different diameters. (d) Incident power density dependent PLQY values (λ_{ex}=514 nm) of QW arrays, NW arrays and thin film counterpart. (e) Radiative

recombination rate versus the inverse NW diameter squared. (f) Non-radiative recombination rate versus the NW surface-to-volume ratio (2/r). (g) Time dependent PLQY values of 5.7nm QW arrays, 250nm NW arrays and thin film counterpart. All those sample are stored under ambient condition (temperature: 23ºC, relative humidity: 18%-40%).

Table 1. Average lifetimes (τ_{ave}), maximum PLQY values, radiative (R_{rad}) and non-radiative (R_{nrad}) recombination rates, and average light outcoupling efficiency for different NW arrays. τ_{ave} is extracted from the double-exponential fitting of PL decays. R_{rad} and R_{nrad} are calculated by using τ_{ave} and PLQY value under the same incident photon flux. The light outcoupling efficiency is averaged by different orientations and positions in the NW arrays.

NWs diameter (nm)	τ_{ave} (ns)	Max PLQY (%)	R_{rad} (s^{-1})	R_{nrad} (s^{-1})	Average light outcoupling efficiency (%)
5.7	4.126	42.6	3.71×10^{7}	2.04×10^{8}	41.35
9.1	6.001	13.1	9.24×10^{6}	1.57×10^{8}	42.17
12.2	8.124	0.87	1.11×10^{6}	1.22×10^{8}	36.77
18.8	8.325	0.78	6.45×10^{5}	1.19×10^{8}	26.05
250	3.039	0.33	6.82×10^{5}	3.28×10^{8}	18.65

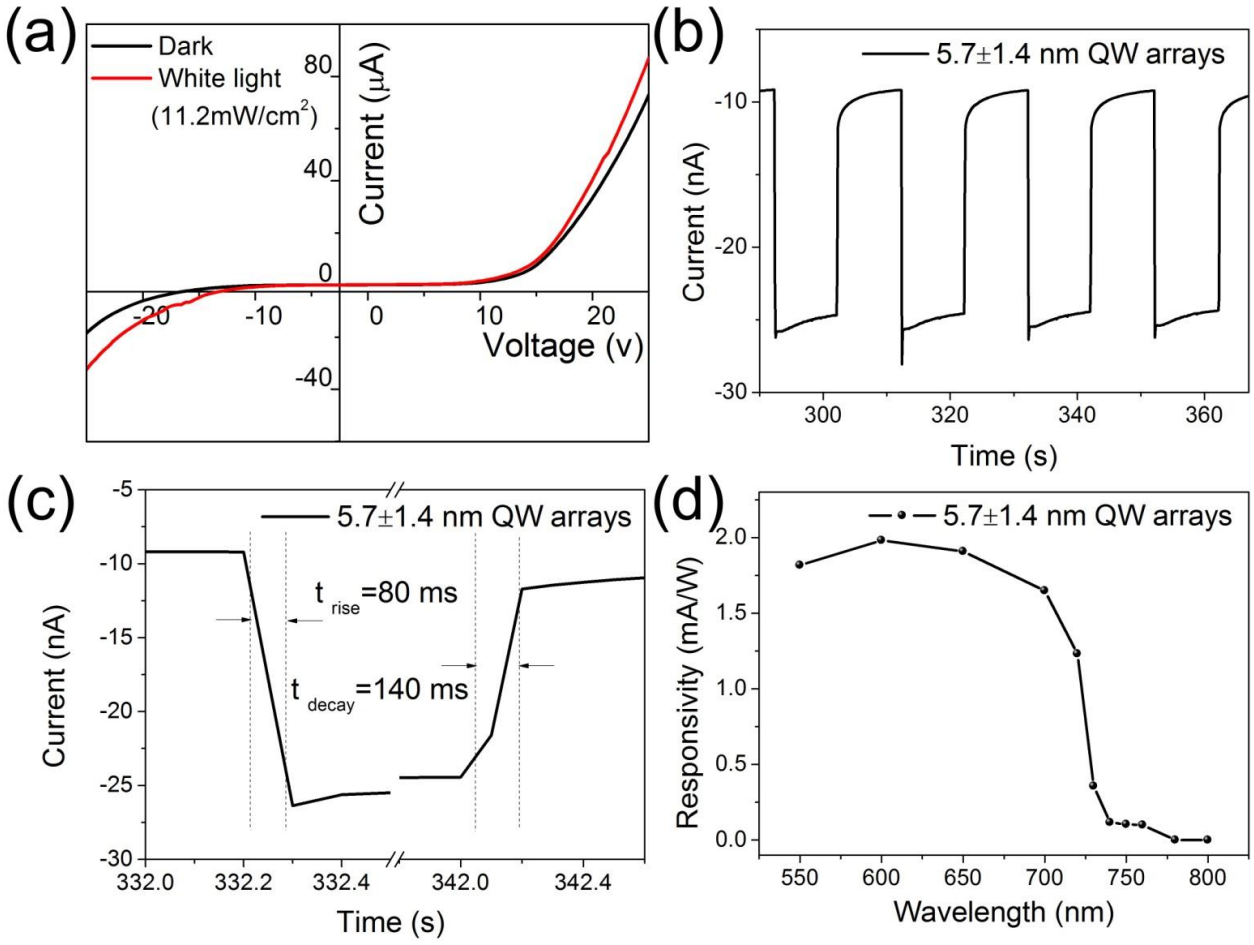

Figure 4. (a) I-V curves under dark condition and white color light illumination (11.2 mW/cm^2) for 5.7±1.4 nm QW arrays based device. (b) Time-domain photoresponses to the same white color light for different diameter $MAPbI_3$ QW arrays based devices under -5 V bias. (c) Response time under the same white light and (d) wavelength-dependent responsivity analysis for 5.7±1.4 nm QW arrays based device with -5 V bias.

Supporting information

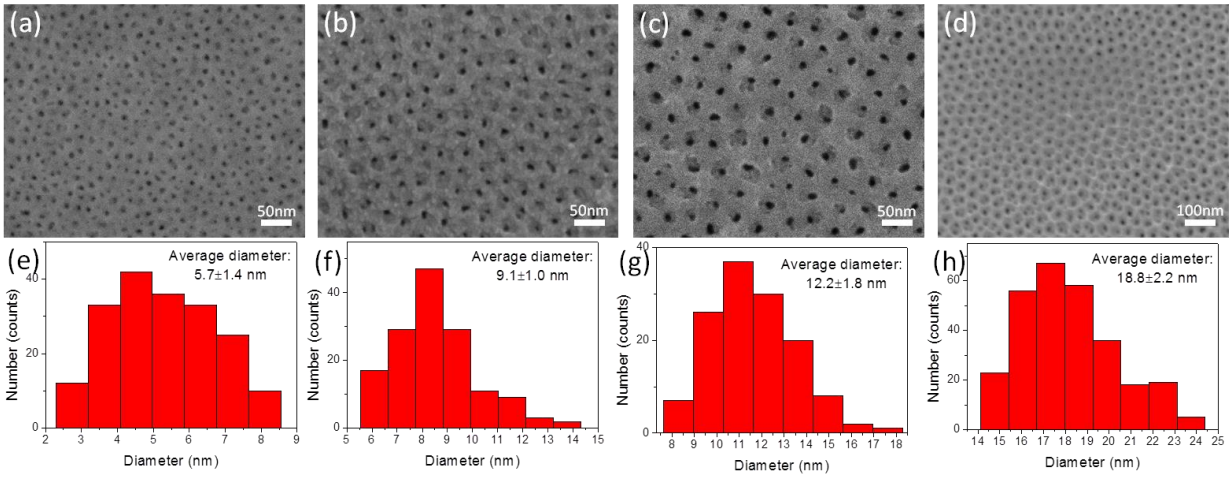

Figure S1. SEM images and statistic pore size distributions of 5 V (a and e), 10 V (b and f), 15 V (c and g), and 20 V (d and h) PAM.

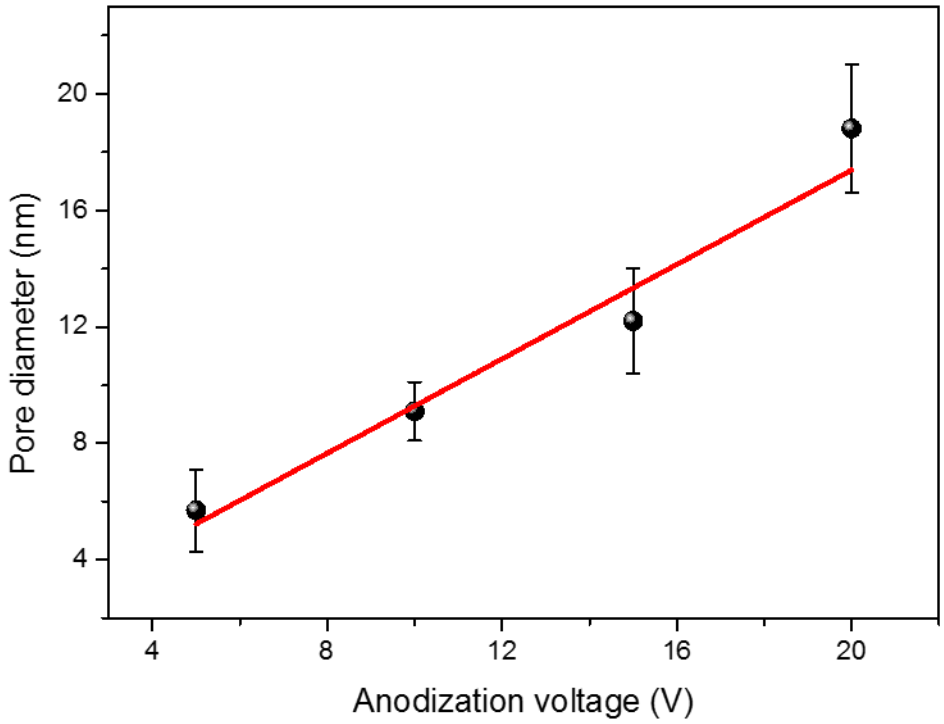

Figure S2. The dependence of PAM pore diameters on the anodization voltages (red dots) and the linear fitting (red line).

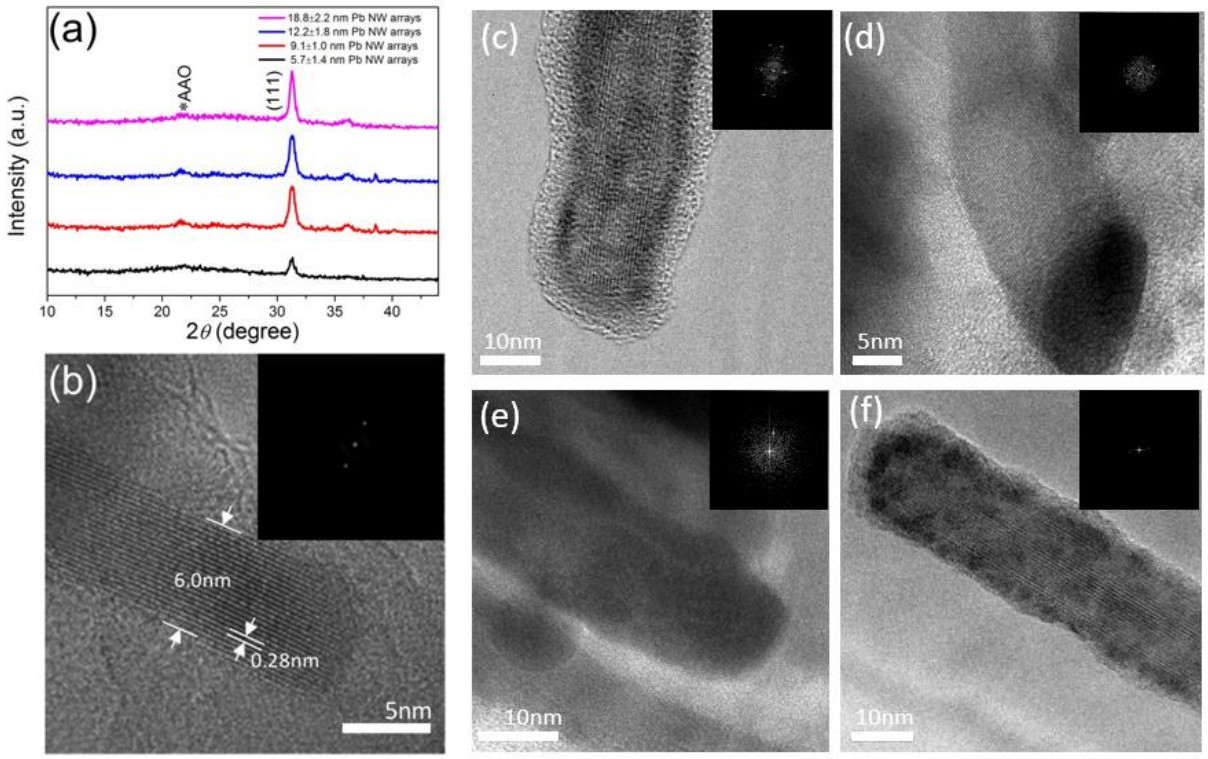

Figure S3. (a) XRD patterns of different Pb NW arrays. TEM images of Pb NWs extracted from (b)5v, (c)10v, (d)15v and (e)20v AAO and a single MAPbI3 QW extracted from 10v AAO. The inserts show the corresponding FFT analysis.

Table S1. Double-exponential fitting results for different NW arrays PL decay profiles.

NWs diameter (nm)	τ_1(ns)	τ_2(ns)	B_1	B_2
5.7nm QWs	2.94	13.13	0.1655	0.02242
9.1nm QWs	3.5	22.76	0.1382	0.02068
12.2nm QWs	4.35	27.29	0.1423	0.02802
18.8nm QWs	4.27	32.07	0.1294	0.0221

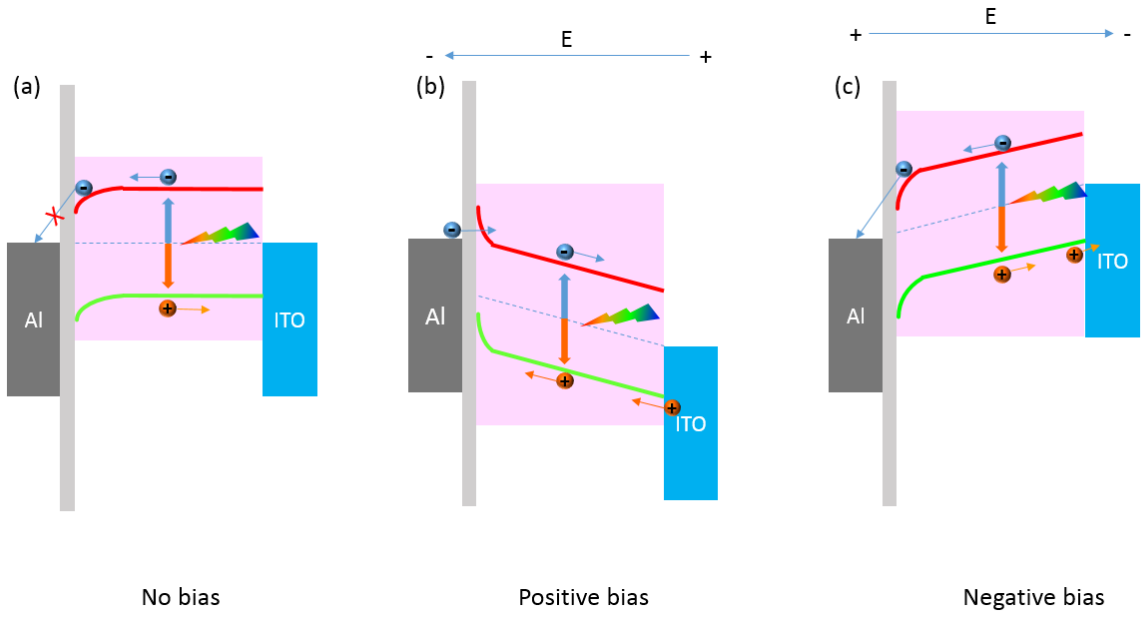

Figure S4. Band alignment diagram for $MAPbI_3$ QW arrays device.

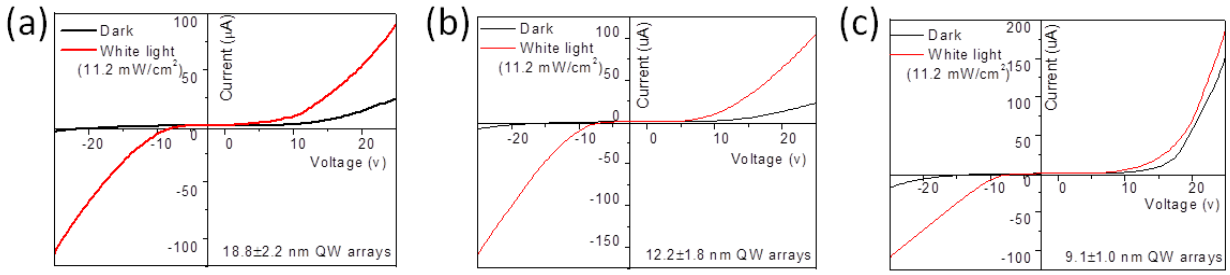

Figure S5. I-V curves under dark condition and white color light illumination (11.2 mW/cm^2) for (a) 18.8 ±2.2 nm, (b) 12.2±1.8 nm, and (c) 9.1±1.0 nm QW arrays based devices.